



# Ecklonia cava based mesoporous activated carbon for high-rate energy storage devices

Kue-Ho Kim<sup>a</sup>, Dong-Yo Shin<sup>b</sup>, Hyo-Jin Ahn<sup>a,b,\*</sup>

<sup>a</sup> Department of Materials Science and Engineering, Seoul National University of Science and Technology, Seoul, 01811, South Korea

<sup>b</sup> Program of Materials Science & Engineering, Convergence Institute of Biomedical Engineering and Biomaterials, Seoul National University of Science and Technology, Seoul, 01811, South Korea

## ARTICLE INFO

### Article history:

Received 8 November 2019

Received in revised form 23 December 2019

Accepted 23 January 2020

Available online 30 January 2020

### Keywords:

Electrical double-layer capacitors

Activated carbon

Ecklonia cava

Mesoporous structure

Rate performance

## ABSTRACT

Activated carbon has received enormous global attention as an electrode material for electrical double layer capacitors (EDLCs) due to its superior electrochemical performance. But while manufacturing high-quality activated carbon as an electrode material, overcoming limitations such as depletion of raw material resources, poor high-rate performance, and cycle stability is still a significant challenge. To address these limitations, we firstly suggest a novel mesoporous activated carbon derived from ecklonia cava (Meso-ACDE) using an acid-base reaction and KOH activation processes. The optimized Meso-ACDE electrode showed a superior specific capacitance of  $182 \text{ F g}^{-1}$  at the current density of  $0.2 \text{ A g}^{-1}$  and a high-rate capacitance of  $154 \text{ F g}^{-1}$  at the current density of  $20.0 \text{ A g}^{-1}$  with an excellent cycling stability up to 2000 cycles. The enhanced electrochemical performance of the Meso-ACDE electrode was mainly attributed to the well-developed mesoporous structure with a high concentration of oxygen related functional groups, which were acquired during the activation process. Thus, we believe that the Meso-ACDE could be a promising alternative to conventional activated carbon for high-performance EDLCs. © 2020 The Korean Society of Industrial and Engineering Chemistry. Published by Elsevier B.V. All rights reserved.

## Introduction

Due to the growing concerns about energy exhaustion, high-performance energy storage devices which are operated by electrochemical reactions have received significant attention due to their efficient energy usage and eco-friendliness [1–3]. Among the various energy storage devices, electrochemical capacitors (ECs) which use activated carbon as the electrode material have attracted enormous scientific consideration for their high power density, fast charge/discharge rate, long cycle life, and wide operating temperature range [4–6]. Moreover, ECs fabricated with activated carbon materials are proposed to be promising devices that can narrow the gap of power and energy density [7–9]. ECs can be broadly categorized into three types according to their energy storage mechanisms [10–12]: (1) electrical double-layer capacitors (EDLCs), (2) pseudo capacitors, and (3) hybrid capacitors. Among these, EDLCs use electrostatic adsorption/desorption

of the charge between the carbon-based materials based on non-faradaic capacitive process.

Currently, most manufacturing processes used to synthesize activated carbon for use as electrode materials utilize pitches, cokes, and coals as source materials. However, these materials are at risk of serious depletion. To overcome this limitation, bioderived activated carbon materials have been adopted recently due to their intrinsic/extrinsic characteristics such as high surface area, low cost, abundance of raw materials, eco-friendliness, and simple synthesis methods [13,14]. When selecting bioderived raw materials, the activation method and conditions are significant factors that can dramatically alter the electrochemical performance according to their resultant pore size and distribution, specific surface area, electrical conductivity, etc. Various natural raw materials such as seaweed [15], grapefruit peel [16], coffee beans [17], firwood [18], and corn grains [19] have been actively studied for high-performance supercapacitor applications. For example, Kishore et al. synthesized porous carbon from coconuts using a KOH activation process. They reported that the activated carbon derived from the coconut kernel showed a high specific capacitance ( $173 \text{ F g}^{-1}$ ) with a large surface area ( $1200 \text{ m}^2 \text{ g}^{-1}$ ) [20]. Redondo et al. demonstrated activated carbon derived from olive pits using KOH activation with a high volumetric capacitance of  $140 \text{ F cm}^{-3}$ , which was attributed to the precisely controlled pore structure [21].

\* Corresponding author at: Department of Materials Science and Engineering, Seoul National University of Science and Technology, Seoul, 01811, South Korea.  
E-mail address: [hjahn@seoultech.ac.kr](mailto:hjahn@seoultech.ac.kr) (H.-J. Ahn).

Moreover, brown algae related raw materials including seaweed, *Undaria pinnatifida* which are large scale inhabitants in the west sea of Korea, are also interesting candidates for supercapacitor application due to their rich initial oxygen content and abundance at sea [22]. However, the critical limitation of bio-derived activated carbon is low mesopore volume fraction, which causes a poor high-rate performance due to the long ionic diffusion pathway [23,24].

Thus, in this paper, we demonstrated mesoporous activated carbon derived from *Ecklonia cava* (EC) for the first time. The mesoporous structure was developed via a sodium hydrogen carbonate - acetic acid reaction (acid-base reaction) and KOH activation. In particular, the acid-base reaction effectively facilitated the KOH activation by extending the activation area. The mesoporous activated carbon derived from EC improved the electrochemical performance, and was attributed to their optimized mesoporous structure, which provided a high specific surface area, maximized oxygen related functional groups, and a short ion diffusion path with a large mesopore volume fraction. To verify the performance enhancement, we identified the relationship between its structural, chemical, morphological, and electrochemical performance.

### Experimental details

The mesoporous activated porous carbon derived from EC (Meso-ACDE) was successfully synthesized using an activation process. First, dried EC (jungbu Co. (Korea)) was washed with nitric acid following a heat treatment at 400 °C for 3 h to eliminate impurities and stabilize the raw material. The collected samples were put into a 0.05 M sodium hydrogen carbonate ( $\text{NaHCO}_3$ ) solution. After stirring for 12 h, 3 vol% of acetic acid ( $\text{CH}_3\text{CO}_2\text{H}$ , Aldrich) was added into the  $\text{NaHCO}_3$  solution to crack the stabilized EC. Then, the resultant sample was dried in an oven at 100 °C after several washing processes using nitric acid and DI water. The prepared sample was mixed with potassium hydroxide

(KOH, SAMCHUN) at the weight ratio of 1:4 ( $W_{\text{sample}}/W_{\text{KOH}}$ ), and then carbonized at 800 °C for 2 h in a nitrogen atmosphere accompanied with KOH activation process. Lastly, the carbonized sample was dried in an oven at 80 °C after washing with hydrochloric acid (HCl, SAMCHUN) and DI water to remove the residue from the activation reaction. For comparison, we prepared carbon derived from EC without any activation process, only with KOH activation process, and commercial activated carbon (thereafter identified as CDE, ACDE, commercial AC, respectively).

The morphology and structural characteristics of the samples were investigated using field-emission scanning electron microscopy (FESEM, Hitachi S-4800). Structural analyses were conducted using X-ray diffraction (XRD, Rigaku D/Max-2500 diffractometer using  $\text{Cu K}\alpha$  radiation), and the chemical bonding states were confirmed via X-ray photoelectron spectroscopy (XPS, ESCALAB 250 equipped with an  $\text{Al K}\alpha$  X-ray source). The porous structure of the sample was examined using the Brunauer-Emmett-Teller (BET) and Barrett-Joyner-Halenda (BJH) methods with  $\text{N}_2$  adsorption isotherms. Electrochemical measurements were performed using the two-electrode system with 6 M KOH solution as the electrolyte. The electrode paste slurries were prepared using the respective active materials, ketjen black (Mitsubishi Chemical, ECP-600JD), and polyvinylidene difluoride (PVDF, Alfa Aesar) in *N*-methyl-2-pyrrolidone (NMP, 99.5%, Aldrich). Then the slurries were dried at 100 °C after being coated onto nickel foam (MTI Korea). Cyclic voltammetry (CV) was carried out using a potentiostat/galvanostat (Ecochemie Autolab, PGST302 N) in the potential range of 0.0–1.0 V, and a charging/discharging test was performed at the current density of 0.2–20.0  $\text{A g}^{-1}$ . The cycling stability was examined up to 2000 cycles at the current density of 1.0  $\text{A g}^{-1}$ .

### Results and discussion

Fig. 1 shows the schematic illustration of the synthetic procedure of Meso-ACDE using the acid-base reaction and KOH activation. Firstly, the dried EC (see Fig. 1(a)) was stabilized in the

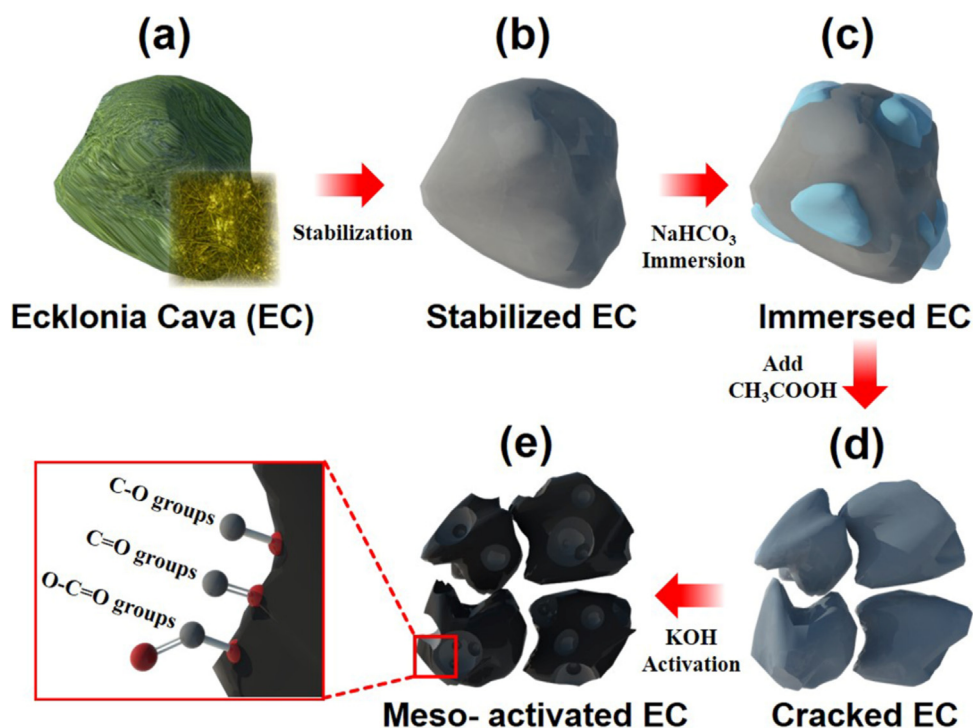


**Fig. 1.** Schematic illustration of the synthesis procedure for Meso-ACDE. (a) ecklonia cava (EC), (b) stabilized EC, (c) immersed EC with  $\text{NaHCO}_3$ , (d) cracked EC, and (e) Meso-ACDE.

air atmosphere to remove the impurities (see Fig. 1(b)). Then, for the acid-base reaction, the stabilized EC was immersed into a sodium hydrogen carbonate solution, followed by the addition of acetic acid (see Fig. 1(c)). As shown in Fig. 1(d), the cracked EC was fabricated after the acid-base reaction, which is attributed to the reaction described by the following equation (see Eq. (1)) [25]:



The acid-base reaction between absorbed sodium hydrogen carbonate and added acetic acid can crack the stabilized EC, leading to the cracked EC form. In other words, the acid-base reaction occurred the cracked EC structure efficiently because of generation of  $\text{CO}_2$  gas due to the added acetic acid. Then, KOH activation accompanied with carbonization was conducted according to the following process in  $\text{N}_2$  atmosphere at  $800^\circ\text{C}$  (see Eq. (2–4)) [26,27]:



Lastly, Fig. 1(e) describes the successfully developed mesoporous structure and surface functional groups, including C—O, C=O, and O—C=O of Meso-ACDE by the synergetic effect of the acid-base reaction and KOH activation processes.

Fig. 2 shows low and high-magnification FESEM images of CDE, ACDE, Meso-ACDE, and commercial AC, respectively. For the case of CDE (see Fig. 2(a, e)), a bulk carbon structure without any pores was observed. ACDE (see Fig. 2(b, f)) presented a porous surface due to the KOH activation process. Interestingly, the Meso-ACDE samples (see Fig. 2(c, g)) demonstrated an optimized mesoporous structure throughout the surface and inner part of the EC. It seems that the cracked morphology of the EC after the acid-base reaction effectively increased the KOH activation area of the stabilized EC, which generated the synergetic effect of the acid-base reaction and KOH activation. In contrast, the commercial AC (see Fig. 2(d, h)) shows a smooth surface with few mesopores as compared to the Meso-ACDE.

Fig. 3 displays the XRD plots used to investigate the crystallinities of all the samples. Broad diffraction peaks of around  $25^\circ$  were detected in all the samples, which correspond to (002) layers of graphite [28,29]. The intensities of the graphite peaks,

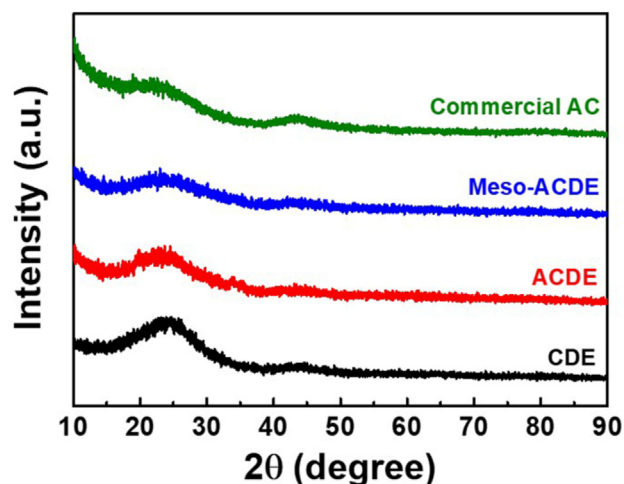


Fig. 3. XRD curves of CDE, ACDE, Meso-ACDE, and commercial AC.

which represent the carbon crystallinity, gradually decreased from the CDE to the Meso-ACDE samples as the porosity increased [30,31]. Moreover, to characterize the chemical bonding states of the samples, XPS measurements were performed, as shown in Fig. 4. The binding energy of C 1s (284.5 eV) was used as a reference. The C 1s XPS core-level spectra of all the samples were divided into four peaks including C—C bonding (at 284.5 eV), C—O bonding (at 286.0 eV), C=O bonding (at 287.2 eV), and O—C=O bonding (at 288.5 eV). Among them, the C—O and C=O peaks represent the binding energy of the hydroxyl groups (—OH) and the O—C=O peaks represent the binding energy of the carboxyl groups (—COOH) [31,32], which are highly relevant to the surface functional groups. As shown in Fig. 4(a–c), the peak intensities which correspond to the oxygen related functional groups gradually increased from CDE to Meso-ACDE. The specific XPS analyses are summarized in Table 1 according to the concentration (%) of the respective peaks. The results indicate that the percentage of the oxygen related surface functional groups increased after the KOH activation. Moreover, Meso-ACDE showed the highest concentration of oxygen related surface functional groups, up to 44.54% (see Table 2), due to the accelerated KOH activation process with the synergetic effect of the acid-base reaction. The increased concentration of the oxygen functional groups on the carbon surface contributed to the cycle stability of the EDLCs as compared to the C—C groups due to the enhanced wettability of the carbon

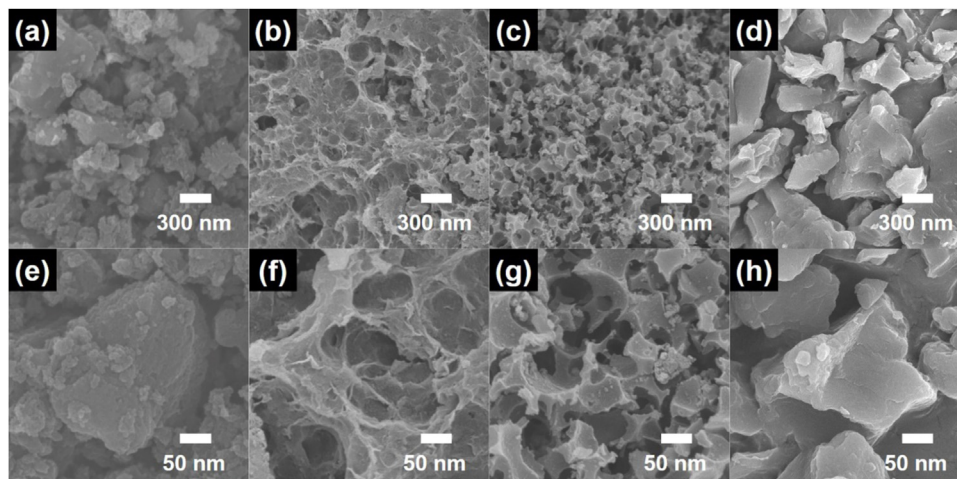


Fig. 2. Low-resolution (a–d) and high resolution (e–h) FESEM images of CDE, ACDE, Meso-ACDE, and commercial AC.

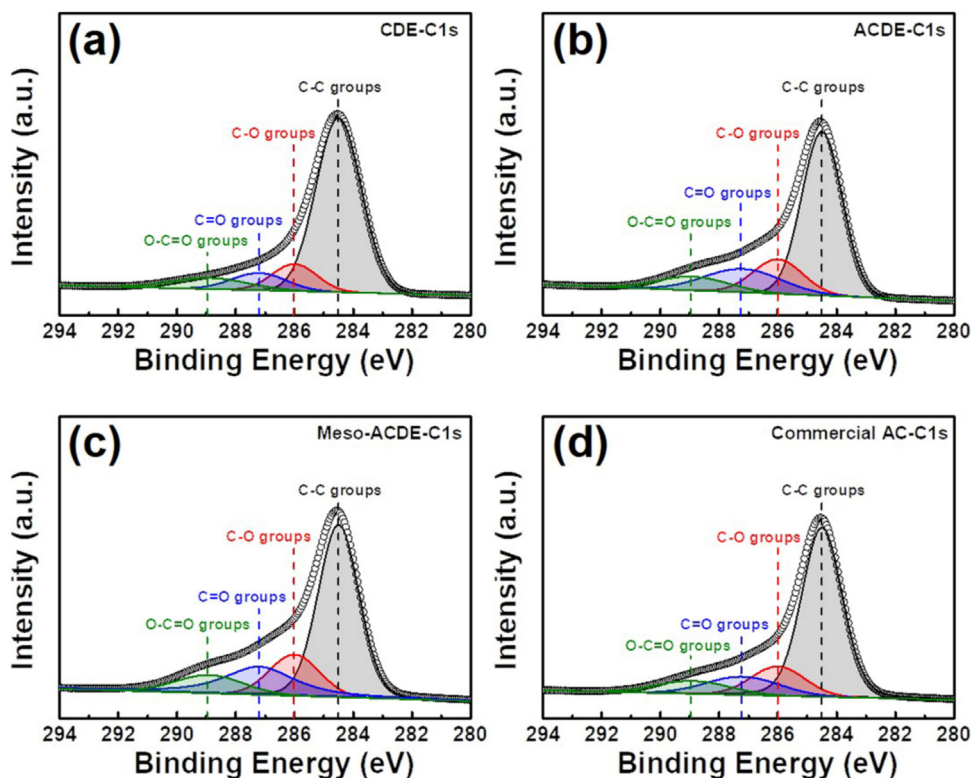


Fig. 4. XPS core-level spectra of C1s for (a) CDE, (b) ACDE, (c) Meso-ACDE, and (d) commercial AC, respectively.

Table 1

Summarized concentration(%) data of XPS results for CDE, ACDE, Meso-ACDE, and Commercial AC.

Samples	C—C (284.5 eV) Concentration (%)	C—O (286.1 eV) Concentration (%)	C=O (287.2 eV) Concentration (%)	O—C=O (288.9 eV) Concentration (%)
CDE	72.45	11.00	8.58	7.95
ACDE	59.73	15.35	16.13	8.78
Meso-ACDE	55.44	16.32	18.98	9.24
Commercial AC	65.65	13.99	11.98	8.36

Table 2

Specific surface area, total pore volume, average pore diameter, and pore volume fraction of CDE, ACDE, Meso-ACDE, and Commercial AC.

Samples	$S_{\text{BET}}$ [ $\text{m}^2 \text{g}^{-1}$ ]	Total pore volume ( $p/p_0=0.990$ ) [ $\text{cm}^3 \text{g}^{-1}$ ]	Average pore diameter[nm]	Pore size distribution	
				$V_{\text{micro}}$ (%)	$V_{\text{meso}}$ (%)
CDE	608	–	–	–	–
ACDE	2596	1.767	2.451	80.2	19.8
Meso-ACDE	2757	1.867	2.723	72.1	27.9
Commercial AC	2197	0.989	1.802	99.1	0.9

surface with the electrolyte, as a high wettability can effectively provide an improved utilization of the carbon surface area and facilitate the ion transfer property at a high current density.

Fig. 5(a–c) show the BET and BJH data of the samples, which were measured using  $\text{N}_2$  adsorption/desorption isotherms to examine their pore structures. According to the International Union of Pure and Applied Chemistry, the pores can be divided into three groups based on their size: micropore (<2 nm), mesopore (2–50 nm), and macropore (>50 nm) [33,34]. In Fig. 5(a), the isotherm of CDE shows the behavior of a bulk structure without pores and the isotherm of commercial AC shows type I behavior, implying the existence of micropores. However, the isotherms of ACDE and Meso-ACDE exhibit type IV behavior, indicating the development of a mesopore structure at high  $\text{N}_2$

pressures ( $P/P_0 > 0.4$ ). Meso-ACDE, especially, showed distinctive isotherm behavior of a mesoporous structure and the highest pore volume within the pore diameter of 2–50 nm (see Fig. 5(b)). The successful development of mesoporous carbon structure is mainly due to the synergetic effects of the acid-base reaction and KOH activation involving multiple chemical reactions. Table 2 summarizes the analysis results of the surface porous structure. The value of the specific surface area gradually increases from  $608 \text{ m}^2 \text{g}^{-1}$  for CDE to  $2596 \text{ m}^2 \text{g}^{-1}$  for ACDE and  $2757 \text{ m}^2 \text{g}^{-1}$  for Meso-ACDE, which is much higher than commercial AC ( $2197 \text{ m}^2 \text{g}^{-1}$ ). This improvement is due to the KOH activation process and the additional acid-base reaction of CDE. As shown in Table 2, the Meso-ACDE presents an optimized mesopore volume fraction of 27.9% as compared to ACDE (19.8%) and commercial AC (0.9%).

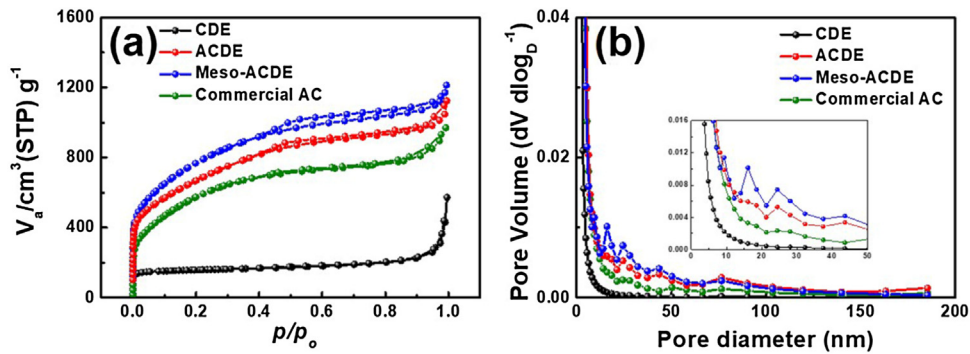


Fig. 5. (a)  $\text{N}_2$  adsorption/desorption isotherms and (b) BJH pore size distribution of CDE, ACDE, Meso-ACDE, and commercial AC.

Therefore, the mesoporous structure was effectively developed using the acid-base reaction of stabilized EC and the KOH activation process during carbonization. Thus, the mesoporous structure of the sample can contribute to a high-rate performance of the EDLCs, providing a favorable ionic diffusion path between the interface of the electrode and electrolyte at a high current density.

To investigate the electrochemical performance, the CV measurements were carried out in the potential range from 0.0 V to 1.0 V, using the potentiostat/galvanostat at a scan rate of  $10\text{ mVs}^{-1}$ . The conventional two-electrode system with prepared electrodes was used in the 6M KOH electrolyte. As shown in Fig. 6(a), all electrodes appeared as rectangular CV curves, implying the presence of the electrical double-layer region at the interface of the electrode and electrolyte. The Meso-ACDE electrodes showed the largest CV curve among all the electrodes due to their large electrical double-layer region with a high specific surface area. Fig. 6(b) shows the charging/discharging tests which were performed at a current density from  $0.2\text{--}20.0\text{ Ag}^{-1}$ . To

calculate the specific capacitance ( $C_{sp}$ ) of all electrodes, the following equation was used (see Eq. (5)) [15,35–37]:

$$C_{sp} = 4I / (m dV/dt) \quad (5)$$

The parameters involved in Eq. (5) are as follows:  $I$  (A) denotes the applied current,  $m$  (g) is the mass of the active materials,  $dV$  is the voltage drop during discharging, and  $dt$  is the discharging time. The specific capacitances of CDE, ACDE, Meso-ACDE, and commercial AC electrodes were  $61, 164, 182,$  and  $175\text{ Fg}^{-1}$ , respectively, at the current density of  $0.2\text{ Ag}^{-1}$ . This superb specific capacitance of the Meso-ACDE electrodes is attributed to its high specific surface area as compared to the other electrodes. In addition, due to the high mesopore volume fraction, the Meso-ACDE electrodes retained their specific capacitance at a high current density with a high capacitance retention of 84.6% ( $154\text{ Fg}^{-1}$  at the current density of  $20.0\text{ Ag}^{-1}$ ). In contrast, the specific capacitance of the commercial AC electrodes decreased rapidly as the current density increased due to their low mesopore volume fraction, which caused a low capacitance retention of 62.8% ( $110\text{ Fg}^{-1}$  at the

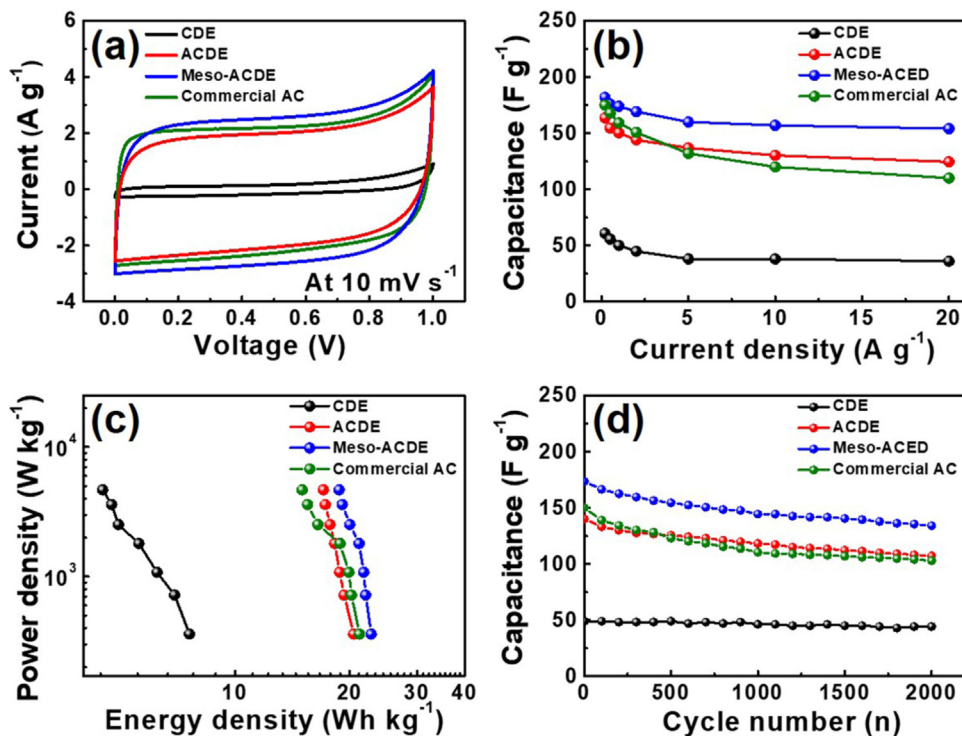


Fig. 6. (a) CV curves of CDE, ACDE, Meso-ACDE, and commercial AC electrodes measured between 0.0 V and 1.0 V at the scan rate of  $10\text{ mVs}^{-1}$ , (b) Specific capacitance at a current density of  $0.2\text{--}20.0\text{ Ag}^{-1}$ , (c) Ragone plots regarding energy and power densities, and (d) Cycling stability at the current density of  $1\text{ Ag}^{-1}$  up to 2000 cycles.

current density of  $20.0 \text{ A g}^{-1}$ ). In other words, the improved high-rate performance of the EDLCs with a high capacitance retention could be mainly attributed to a high mesopore volume fraction, which could facilitate a favorable ion transport with a short ion diffusion path [10,38]. Consequently, these results indicate that the mesoporous structure at the Meso-ACDE electrodes was optimized. Fig. 6(c) shows the calculated energy density ( $E, \text{ Wh kg}^{-1}$ ) and power density ( $P, \text{ W kg}^{-1}$ ) as a Ragone plot using specific capacitance values with the following equation [39,40]:

$$E = C_{sp} V^2 / 8 \quad (6)$$

$$P = E / dt \quad (7)$$

In Eqs. (6,7),  $C_{sp}$ ,  $V$ , and  $dt$  represent the specific capacitance, discharging voltage, and the total discharge time, respectively. The Ragone plots of all the electrodes display an increase in the power density as the energy density decreases. As shown in Fig. 6(c), the Meso-ACDE electrodes demonstrated a high energy density of  $22.7\text{--}18.7 \text{ Wh kg}^{-1}$  in the power density range of  $360\text{--}4680 \text{ W kg}^{-1}$ . Meanwhile, the commercial AC electrodes show a rapid decrease in the energy density ( $21.2\text{--}15.0 \text{ Wh kg}^{-1}$ ) as the power density increased, due to their low mesopore volume fraction. To investigate the cycle stability of all the electrodes, sequential charging and discharging tests up to 2000 cycles at fixed current density of  $1.0 \text{ A g}^{-1}$  (see Fig. 6(d)) were conducted. The Meso-ACDE electrodes showed a superior cycle stability with a specific capacitance of  $134 \text{ F g}^{-1}$  after 2000 cycles (capacitance retention of 77.3%), whereas, the commercial AC electrodes showed a poor cycle stability with a specific capacitance of  $101 \text{ F g}^{-1}$  after 2000 cycles (capacitance retention of 67.2%). These results indicate that the high concentration of oxygen related functional groups could effectively facilitate a favorable ion transfer between electrodes during the charging and discharging process, leading to an excellent cycle stability. The Nyquist plots of all the electrodes at the open circuit potential are displayed in Fig. 7. At the high-frequency range (see inset of Fig. 7), which implies the inner resistance of the prepared electrode, all electrodes showed similar curves. However, at the low-frequency range, the linear region of the graph, which signifies the ionic diffusion ability within the electrode, was split [22,41]. The steepest slope occurred for the Meso-ACDE among all the electrodes, indicating that the optimized mesoporous structure affected the ion diffusion performance with a short ion diffusion path.

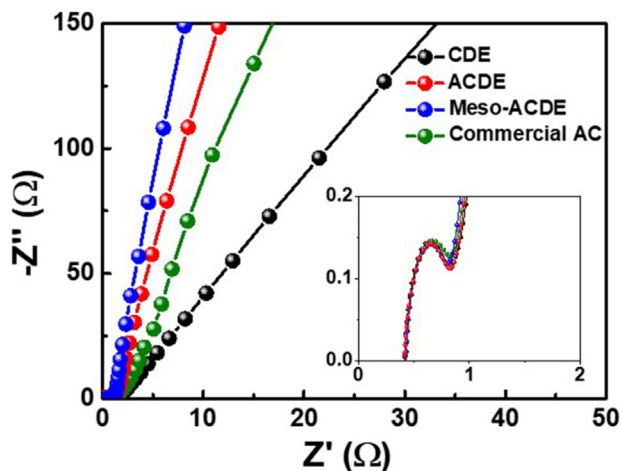


Fig. 7. Nyquist plots of CDE, ACDE, Meso-ACDE, and commercial AC at the open circuit potential.

Thus, the excellent electrochemical performance of Meso-ACDE electrodes fabricated with an acid-base reaction and KOH activation was because of the high specific surface area and optimized mesoporous structure. Firstly, the high specific surface area contributed to the high specific capacitance at a low current density. Secondly, the high concentration of oxygen related functional groups contributed to the enhancement of the high-rate cycle stability. Lastly, the successful development of the mesoporous structure provided a favorable ionic diffusion path, leading to a noticeable high-rate capacitance. According to these results, activated carbon with a mesoporous structure derived from EC could be a great candidate for usage in high-performance EDLCs.

## Conclusion

In this paper, activated carbon derived from EC was successfully synthesized using an acid-base reaction for stabilized EC and KOH activation during the carbonization process. Meso-ACDE samples demonstrated a high specific surface area of  $2757 \text{ m}^2 \text{ g}^{-1}$  with large mesopore volume fraction of 27.9% because of the synergetic effects of the acid-base reaction and KOH activation process. Moreover, the concentration of the oxygen related functional groups was maximized (44.5%) in the Meso-ACDE samples. The superior electrochemical performance of the Meso-ACDE electrodes, including high specific capacitance of  $182 \text{ F g}^{-1}$  at the current density of  $0.2 \text{ A g}^{-1}$ , high-rate performance ( $154 \text{ F g}^{-1}$  at the current density of  $20.0 \text{ A g}^{-1}$ ), and cycle stability (capacitance retention of 77.3% after 2000 cycles), were mainly attributed to the following results: (1) the high specific surface area due to the acid-base reaction and KOH activation enables a high specific capacitance at a low current density; (2) maximized oxygen related functional groups lead to an improvement of the high-rate cycle stability; (3) a short ion diffusion path with a large mesopore volume fraction effectively enhanced the high-rate capacitance. Therefore, the Meso-ACDE electrode could be a good suggestion for high-performance EDLCs.

## Declaration of interests

The authors declare that they have no known competing financial interests or personal relationships that could have appeared to influence the work reported in this paper.

## Acknowledgements

This work was supported by the National Research Foundation of Korea (NRF) grant funded by the Korea government (MSIT) (No. 2019R1 A2 C1005836)

## References

- [1] W. Raza, F. Ali, N. Raza, Y. Luo, K.-H. Kim, J. Yang, S. Kumar, A. Mehmood, E. Kwon, *Nano Energy* 52 (2018) 441.
- [2] S. Faraji, F.N. Ani, *Renew. Sust. Energ. Rev.* 42 (2015) 823.
- [3] F. Sun, J. Gao, X. Liu, X. Pi, Y. Yang, S. Wu, *Appl. Surf. Sci.* 387 (2016) 857.
- [4] M. Inagaki, H. Konno, O. Tanaike, *Carbon* 195 (2010) 7880.
- [5] I.G. Inal, S.M. Holmes, E. Yagmur, N. Ernumcu, A. Banford, Z. Aktas, *J. Ind. Eng. Chem.* 61 (2018) 124.
- [6] G.P. Awasthi, D.P. Bhattarai, B. Maharjan, K.-S. Kim, C.H. Park, C.S. Kim, *J. Ind. Eng. Chem.* 72 (2019) 265.
- [7] P. Simon, Y. Gogotsi, B. Dunn, *Science* 343 (2014) 1210.
- [8] P. Simon, Y. Gogotsi, *Nat. Mater.* 7 (2008) 845.
- [9] J.R. Miller, *Appl. Surf. Sci.* 460 (2018) 3.
- [10] G.-H. An, B.-R. Koo, H.-J. Ahn, *Phys. Chem. Chem. Phys.* 18 (2016) 6587.
- [11] G.-H. An, D.-Y. Lee, H.-J. Ahn, *J. Mater. Chem. A* 5 (2017) 19714.
- [12] H. An, Y. Wang, X. Wang, N. Li, L. Zheng, *J. Solid State Electrochem.* 14 (2010) 651.
- [13] I.G. Inal, S.M. Holmes, A. Banford, Z. Aktas, *Appl. Surf. Sci.* 357 (2015) 696.
- [14] R.-J. Mo, Y. Zhao, M. Wu, H.-M. Xiao, S. Kuga, Y. Huang, J.-P. Li, S.-Y. Fu, *RSC Adv.* 6 (2016) 59333.

- [15] H. Wang, Z. Xu, A. Kohandehghan, Z. Li, K. Cui, X. Tan, T.J. Stephenson, C.K. King'ondeu, C.M.B. Holt, B.C. Olsen, J.K. Tak, D. Harfield, A.O. Anyia, D. Mitlin, *ACS Nano* 7 (2013) 5131.
- [16] Y.-Y. Wang, B.-H. Hou, H.-Y. Lü, C.-L. Lü, X.-L. Wu, *ChemistrySelect* 1 (2016) 1441.
- [17] T.E. Rufford, D. Hulicova-Jurcakova, Z. Zhu, G.Q. Lu, *Electrochem. Commun.* 10 (2008) 1594.
- [18] F.-C. Wu, R.-L. Tseng, C.-C. Hu, C.-C. Wang, *J. Power Source* 138 (2004) 351.
- [19] M.S. Balathanigaimani, W.-G. Shim, M.-J. Lee, C. Kim, J.-W. Lee, H. Moon, *Electrochem. Commun.* 10 (2008) 868.
- [20] B. Kishore, D. Shanmugasundaram, T.R. Penki, N. Munichandraiah, *J. Appl. Electrochem.* 44 (2014) 903.
- [21] E. Redondo, J. Carrertero-González, E. Goikolea, J. Ségalini, R. Mysyk, *Electrochim. Acta* 160 (2015) 178.
- [22] E. Raymundo-Piñero, M. Cadek, F. Béguin, *Adv. Funct. Mater.* 19 (2009) 1032.
- [23] G.-H. An, D.-Y. Lee, H.-J. Ahn, *J. Ind. Eng. Chem.* 65 (2018) 423.
- [24] W. Yu, H. Wang, S. Liu, N. Mao, X. Liu, J. Shi, W. Lui, S. Chen, X. Wang, *J. Mater. Chem. A* 4 (2016) 5973.
- [25] V. Keishnan, S. Sasikumar, F.P. Dass, R. Vijayaraghavan, *Trends Biomater. Artif. Organs.* 24 (2010) 139.
- [26] H. Zhang, Z. Mo, R. Guo, N. Liu, M. Yan, R. Wang, H. Feng, X. Wei, *J. Mater. Res.* 15 (2019) 1200.
- [27] T. Otowa, R. Tanibata, M. Itoh, *Gas Sep. Purif.* 7 (1993) 241.
- [28] G.-H. An, H.-J. Ahn, *J. Power Source* 272 (2014) 828.
- [29] G.-H. An, E.-H. Lee, H.-J. Ahn, *J. Alloy. Compd.* 682 (2016) 746.
- [30] D.-Y. Lee, G.-H. An, H.-J. Ahn, *J. Ind. Eng. Chem.* 52 (2017) 121.
- [31] H. Chen, G. Wang, L. Chen, B. Dai, F. Yu, *Nanomaterials* 8 (2018) 412.
- [32] G.-H. An, H.-J. Ahn, *J. Electroanal. Chem.* 744 (2015) 32.
- [33] E. Raymundo-Piñero, F. Leroux, F. Béguin, *Adv. Mater.* 18 (2006) 1877.
- [34] C. Largeot, C. Portet, J. Chmiola, P.-L. Taberna, Y. Gogotsi, P. Simon, *J. Am. Chem. Soc.* 130 (2008) 2730.
- [35] H. Sun, W. He, C. Zong, L. Lu, *ACS Appl. Mater. Interfaces* 5 (2013) 2261.
- [36] M. Biswal, A. Banerjee, M. Deo, S. Ogale, *Energy Environ.* 6 (2013) 1249.
- [37] C. Long, X. Chen, L. Jiang, L. Zhi, Z. Fan, *Nano Energy* 12 (2015) 141.
- [38] G.-H. An, H.-J. Ahn, W.-K. Hong, *J. Power Source* 274 (2015) 536.
- [39] J.-W. Lang, X.-B. Yan, W.-W. Liu, R.-T. Wang, Q.-J. Xue, *J. Power Source* 204 (2012) 220.
- [40] X. Yang, L. Zhang, F. Zhang, T. Zhang, Y. Huang, Y. Chen, *Carbon* 72 (2014) 381.
- [41] G.-H. An, J.I. Sohn, H.-J. Ahn, *J. Mater. Chem. A* 4 (2016) 2049.